The Optical Properties of Equatorial Cirrus from Observations in the ARM Pilot Radiation Observation Experiment

C. M. R. PLATT,* S. A. YOUNG, P. J. MANSON,+ G. R. PATTERSON, S. C. MARSDEN, AND R. T. AUSTIN*

CSIRO Division of Atmospheric Research, Aspendale, Victoria, Australia

J. H. CHURNSIDE

NOAA/ETL, Boulder, Colorado

(Manuscript received 28 March 1997, in final form 26 September 1997)

ABSTRACT

The optical properties of equatorial cirrus were studied during a three-week period of the ARM Pilot Radiation and Observation Experiment at Kavieng, Papua New Guinea, in January and February 1993. The experiment consisted of vertical lidar (532 nm) and passive infrared filter radiometer (10.84 μm) observations of cirrus clouds. The observations gave values of cloud height, depth, structure, infrared emittance, infrared absorption, and visible optical depth and linear depolarization ratio. A standard lidar–radiometer analysis, with some improvements, was used to calculate these quantities. The cirrus was found to vary in altitude from a maximum cloud top of 17.6 km to a minimum cloud base of 6 km with equivalent temperatures of -82°C to -7°C respectively. The cirrus also varied widely in depth (0.7 to 7.5 km). The mean emittance (for each temperature interval) of the cooler clouds was found to be higher than that observed previously at tropical and midlatitude sites and at equivalent temperatures. The mean infrared absorption coefficients were similar to those of midlatitude clouds, except at the extreme temperature ranges, but were higher than those observed in tropical synoptic clouds over Darwin. Infrared optical depths varied from 0.01 to 2.4 and visible optical depths from 0.01 to 8.6.

Plots of integrated attenuated backscatter versus infrared emittance, for various ranges of cloud temperature, showed characteristic behavior. Values of the measured quantity $k/2\eta$, where k is the visible backscatter to extinction ratio and η a multiple scattering factor, were found to increase with temperature from 0.14 at -70°C to 0.30 at -20°C.

Values of the quantity $2\alpha\eta$, where α is the ratio of visible extinction to infrared absorption coefficient, varied from about 1.7 to 3.8, depending somewhat on the cloud temperature. Deduced values of α were as high as 5.3 at the lower temperature ranges, indicating smaller particles.

The lidar integrated attenuated depolarization ratio Δ decreased with temperature, as found previously in midlatitude cirrus. Values of Δ varied from 0.42 at -70°C to 0.18 at -10°C. Data obtained from the NOAA/ETL microwave radiometer gave values of water path, varying from 4 to 6 cm precipitable water. A value of the water vapor continuum absorption coefficient at 10.84 μm equal to 9.0 ± 0.5 g^{-1} cm^2 atm^{-1} was obtained in agreement with previous observations.

1. Introduction

This paper describes results obtained in an equatorial region of the tropical West Pacific (TWP) using the lidar–radiometer (LIRAD) method of ground-based remote sensing. The method was developed by Platt (1973, 1979, the latter hereafter referred to as P1) with some extensions due to Young (1995). The results presented here were obtained as part of the Atmospheric Radiation Measurement (ARM) program in an experiment called the ARM Pilot Radiation and Observation Experiment (PROBE) held in Kavieng, New Ireland, Papua New Guinea (PNG). This experiment in turn was part of the Tropical Ocean Global Atmosphere Coupled Ocean–Atmosphere Response Experiment.

The aim of the experiment was to acquire a dataset on the optical and structural properties of cirrus clouds at an equatorial site at 2°S latitude. The cloud properties could then be compared with those obtained in midlatitude and tropical regions (e.g., Platt et al. 1987, hereafter referred to as P6). The data would also provide a preliminary set to compare with data that will be obtained at the ARM TWP long-term observation site at Manus Island, situated some 400 km west-northwest of Kavieng.

* Current affiliation: Department of Atmospheric Science, Colorado State University, Fort Collins, Colorado.

+ Current affiliation: Department of Physics, University of Otago, Dunedin, New Zealand.

Corresponding author address: Dr. C. Martin R. Platt, Department of Atmospheric Science, Colorado State University, Fort Collins, CO 80523.
E-mail: martin@atmos.colostate.edu

The importance of clouds in determining both present and future global climates is well recognized. Large programs such as the Global Energy and Water Cycle Experiment and the U.S. Department of Energy ARM Program have been set up to study cloud properties. Thin cirrus ice cloud causes a significant warming of the equilibrium climate, particularly in the Tropics. In contrast, clouds of higher optical depths, such as deep convective clouds, deep frontal clouds, and boundary-layer stratus, can cause an appreciable cooling (e.g., Cess et al. 1990; Stephens and Greenwald 1991). Equatorial cirrus is the coldest class of cloud on the planet and is found over the world's warmest waters. It therefore has the potential to cause the greatest warming of the equilibrium climate by cloud–radiation interactions (e.g., Ramaswamy and Ramanathan 1989).

Recent global circulation models predict an increase in optical depths of cirrus clouds with global warming (e.g., Roeckner 1988). Thus a knowledge of the optical properties of cirrus clouds is crucial for predictions of future climates (e.g., Platt and Harshvardhan 1988). The significance of tropical cirrus clouds has been highlighted recently through their possible control of the sea surface temperature in the TWP (Ramanathan and Collins 1991). The temperature and stability of the atmosphere containing cirrus clouds will similarly be affected (Arking and Ziskin 1994). Prabhakara et al. (1991) have detected extensive sheets of thin cirrus covering tropical regions, particularly the TWP.

The earliest lidar observations of tropical cirrus were probably those of Davis (1971) with an aircraft-mounted lidar. Uthe and Russell (1976) also observed some high-altitude cirrus from Kwajalein Atoll with ground-based lidar. Griffith et al. (1980) made some aircraft in situ measurements during the GARP Tropical Atlantic Experiment. Heymsfield (1986) described particles in a very cold cirrus cloud obtained from aircraft observations. Platt et al. (1984, hereafter referred to as P5) observed cirrus clouds at Darwin with the LIRAD method. Knollenberg et al. (1993) observed high number densities of ice crystal clouds in tropical cumulonimbus anvils from aircraft in situ measurements. Heymsfield and McFarquhar (1996) recently made more extensive aircraft observations of tropical cirrus particle size distributions during the Central Equatorial Pacific Experiment (CEPEX).

The LIRAD method of analysis is able to give detailed results on cirrus optical properties and microphysics. The basic quantities measured are the cloud backscatter coefficient at the lidar wavelength (532 nm for these observations) and the cloud infrared radiance measured at a narrow band of wavelengths (mostly 10.3–11.3 μm). The cloud height and depth are retrieved by lidar and the cloud temperatures are obtained from radiosonde data. Derived from these data are the infrared emittance at the IR wavelength and the visible optical depth at the lidar wavelength. These quantities can be related theoretically to the total graybody IR emittance and the equivalent flux emittance (Platt and Stephens 1980), the solar optical depth and the solar albedo, thus obtaining the complete radiative properties of the cirrus.

The value of the lidar-derived cloud integrated backscatter for unity infrared emittance also gives a measure of the cloud particle scattering phase function in the backscatter direction. This leads to information on ice crystal habit. The ratio of visible extinction to IR absorption in turn gives information on effective cloud particle size (e.g., P1).

The cloud phase can also be obtained from the lidar linear depolarization ratio, which has values from 0.2 to 0.5 in ice clouds, but less than 0.03 in thin water clouds. This ratio is also small for horizontally aligned plate crystals observed in the vertical (e.g., Platt 1978).

Instrumentation and observations are described in section 2 and the theory of the LIRAD method is outlined in section 3. Section 4 describes the calibration of the lidar and infrared data. The calculation of the optical quantities is described in section 5. Results are given in section 6, followed by a discussion in section 7 and some conclusions in section 8. Appendix A describes the theory of radiometric detection and gives a description of how the IR radiometers are aligned and balanced. Errors of measurement are discussed in appendix B.

2. Instrumentation and observations

Observations were made at the PNG Meteorological Department's observational site near the Kavieng airport. Kavieng is situated at the northwest end of New Ireland, PNG, at 2.5°S, 152°E. The CSIRO instrumentation was operational from 18 January to 5 February 1993.

Other instruments at the site in PROBE that were utilized in this study were an IR interferometer (Shaw et al. 1995) and microwave radiometer, the latter which measured the precipitable water vapor and liquid water paths (Westwater et al. 1995). Both instruments were operated by NOAA/ETL, Boulder, Colorado. There were also radiosondes and radioacoustic sounders and surface flux-measuring equipment.

The CSIRO equipment consisted of a three-wavelength polarizing lidar operating at 532 nm and two infrared narrow-beam filter radiometers. The equipment characteristics are given in Table 1. The instruments were operated viewing in the zenith. The ARM and CSIRO radiometers were operated at 1- and 10-s time constant respectively. The lidar was operated in either a single or a dual detector mode. When a single photomultiplier (PMT) detector was used, the amplified signal was routed simultaneously to two input channels on the signal digitizer. Different sensitivities were used on the two channels in order to increase the dynamic range of the recorded signal beyond the 8-bit limitation of the digitizer (Young 1995). In this mode, a single polarizer set to the parallel, perpendicular, or out position was inserted into the optical path while a number of signals

TABLE 1. Instrument characteristics.

Instrument	Parameter	Value
Lidar	Wavelengths	1064, 532, 355 nm
	Pulse energies	360, 190, 95 mJ
	Pulse widths	8, 6, 5 ns
	Pulse repetition frequency	10 Hz (optimum)
	Telescope diameter	40 cm
	Telescope field of view	2 mrad (usual)
	Detectors	2 × Thorn EMI 9816B photomultipliers
CSIRO/ARM Radiometer	Wavelengths	8.62 ± 0.2, 10.86 ± 0.25, 12.04 ± 0.27 μm
	Aperture	4 cm
	Field of view	5 to 20 mrad
	Detector	HgCdTe, LN cooled
	Minimum detectable radiance	3.67×10^{-3} W m^{-2} sr^{-1} Hz$^{-1/2}$
CSIRO Mark II Radiometer	Wavelength	10.84 ± 0.5 μm
	Aperture	4 cm
	Field of view	4 to 20 mrad
	Detector	Unicam Golay cell
	Minimum detectable radiance	1.34×10^{-1} W m^{-2} sr^{-1} Hz$^{-1/2}$

were averaged. For lower clouds that produced stronger signals, the optical signal was split using a polarizing beam splitter and routed to two photomultiplier detectors, each connected to a single channel of the digitizer.

The new ARM radiometer (Platt et al. 1993) was intended as the primary radiometer for obtaining cloud radiance. However, liquid nitrogen necessary for the cooled HgCdTe detector was available for only part of the time, and the CSIRO Mark II radiometer (e.g., Platt 1971) was used for most of the observations.

The equipment was installed in an ARM portable laboratory built into a sea container (Seatainer), and the lidar and ARM radiometer observed vertically through two hatches in the roof. The CSIRO Mark II radiometer had to be operated outside the Seatainer. Problems with heat and direct sunlight during daylight hours meant that the radiometer had to be relocated during the day. The ARM radiometer was operated in the 8.62-μm and 10.86-μm filter bands and was used mainly for comparisons with the ETL interferometer. However, comparisons with the Mark II were also made on one day.

Observations were taken whenever there were cirrus clouds in the zenith sky that were not obscured by lower clouds. The optical axes of the lidar and radiometer were aligned in the zenith. The lidar fired at 30-s intervals and at approximately five pulses per second. Up to 256 pulses were averaged (for that case, at 10 Hz), while the radiometer recorded continuously, the data being stored on a PC computer. The lidar firing and data acquisition sequences were controlled by a PC, the data being eventually transferred to a larger disk storage facility. Because of typical large changes in cloud backscatter signal strength between lidar shots, the data recording had to be monitored carefully to prevent saturation of the digitizer.

The infrared data were compared with the relevant lidar profiles. The average time in the lidar's firing cycle was used for the comparison.

A summary of dates and times of observation is given in Table 2, together with mean cirrus properties. There were three good days of observation when cirrus clouds were present for most of the day. On those days, there was very little convective activity and no thunderstorms nearby. Apart from periods of small cumulus, wide-

TABLE 2. Mean properties of the cloud systems studied.

Date	Number of lidar profiles	Time interval (local time)	Mean cloud base altitude (km)	Mean cloud depth (km)	Midcloud temperature (°C)	Mean absorption emittance
24 Jan	35	0906–1011	11.96	4.85	−68.0	0.627
24 Jan	38	1523–1637	12.41	4.13	−68.5	0.270
24 Jan	27	2116–2243	11.57	4.83	−65.2	0.322
26 Jan	31	1051–1224	10.74	4.62	−55.2	0.518
26 Jan	18	1618–1659	10.20	5.01	−52.6	0.479
29 Jan	21	1358–1506	11.19	3.86	−58.2	0.431
3 Feb	63	0911–1116	8.11	5.22	−35.8	0.545
3 Feb	4	1140–1150	7.62	2.78	−21.9	0.801
3 Feb	34	1351–1503	7.70	2.49	−19.5	0.735
3 Feb	13	1612–1638	7.07	2.15	−17.4	0.476
3 Feb	6	2109–0119	8.87	3.99	−39.9	0.326
4 Feb	69	0837–1144	11.24	2.58	−53.2	0.181
4 Feb	45	1333–1514	9.58	2.69	−39.8	0.475
4 Feb	26	1608–1653	11.12	1.92	−49.3	0.157

spread cirrus was almost continuously observable. None of the cirrus clouds observed at Kavieng were associated directly with thunderstorm anvils. In such cases, low clouds invariably obscured the anvils.

Upper-air radiosonde data were available at 6-hourly intervals from the site, allowing for reasonably accurate cloud temperatures and humidities at intervening times. The NOAA/ETL microwave radiometer measured the total water vapor path and total liquid water path continuously in the zenith. The measured water vapor path agreed to within 4% on average with the water path calculated from the radiosonde data for the time periods when cirrus was observed. This figure was taken as the level of uncertainty in the humidity data.

3. Theoretical considerations

a. General definitions and equations

The treatment of the data, and relevant equations, is broadly similar to previous cases where the LIRAD method was used (P1; Platt and Dilley 1981, hereafter referred to as P4; P5; P6). However, with the use here of a 532-nm lidar, instead of a 694-nm lidar, a term for molecular scatter was also included implicitly in the equations. The isotropic cloud backscatter to extinction ratio k is defined as

$$k = \frac{B_c(\pi)}{\sigma_c}, \tag{1}$$

where $B_c(\pi)$ and σ_c are the cloud isotropic backscatter coefficient and volume extinction coefficient respectively. (The extinction to backscatter ratio formulation is often used in lidar retrieval theory, being the reciprocal of k multiplied by 4π: the so-called lidar ratio.) The total attenuated isotropic backscatter coefficient $B'(\pi, z)$ from the cloudy and molecular components at altitude z can be written (assuming that aerosol attenuation and backscatter can be ignored and that backscatter values have been corrected for attenuation between the cloud and the ground):

$$\begin{aligned} B'(\pi, z) &= B'_c(\pi, z) + B'_m(\pi, z) \\ &= (B_c(\pi, z) + B_m(\pi, z)) \\ &\quad \times \exp\left[-2\int_{z_b}^{z} (\eta(z')\sigma_c(z') + \sigma_m(z'))\, dz'\right], \end{aligned} \tag{2}$$

where subscripts c and m refer to cloud particles and atmospheric molecules respectively, η is a multiple scattering factor, and z_b is cloud-base altitude. It is assumed that multiple scattering between molecules is negligible and that photons scattered by molecules undergo multiple scattering by clouds that is again defined by η.

Here $B_c(\pi, z)$ can be retrieved from (2) either analytically (Fernald 1984) or iteratively (P1). The latter treatment, with some modifications, is used here (see section 5c). When the effects of molecular scatter have been allowed for, the well-known equation for integrated attenuated backscatter, $\gamma'(\pi)$, can be obtained (P1, P6):

$$\gamma'(\pi) = \frac{k}{2\eta}\left[1 - \exp\left(-2\eta\int_{z_b}^{z_t} \sigma_c(z)\, dz\right)\right], \tag{3}$$

where z_t is cloud-top altitude. In (3), η is assumed to be independent of z (P6).

The infrared optical depth δ_a at the filter wavelengths is defined by

$$\delta_a = \int_{z_b}^{z_t} \sigma_a(z)\, dz, \tag{4}$$

where $\sigma_a(z)$ is the volume absorption coefficient. The visible optical depth δ_c at the lidar wavelength can similarly be defined in terms of the extinction coefficient σ_c.

The infrared absorption emittance ε_a is given by

$$\varepsilon_a = 1 - \exp(-\delta_a). \tag{5}$$

The ratio α is defined by

$$\alpha = \sigma_c(z)/\sigma_a(z). \tag{6}$$

Equation (3) can then be written (P1):

$$\gamma'(\pi) = \frac{k}{2\eta}\left[1 - \exp\left(-2\eta\alpha \log\frac{1}{1 - \varepsilon_a}\right)\right]. \tag{7}$$

The implications of a constant η with cloud depth are discussed later.

As in previous work (P4, P6), a quantity Δ is defined that represents the lidar-derived linear depolarization ratio $\Delta(z)$, at an altitude z, integrated over cloud depth:

$$\Delta = \frac{\gamma'(\pi)_\perp}{\gamma'(\pi)_\parallel}, \tag{8}$$

where the subscripts signify perpendicular and parallel polarization components. Here $\Delta(z)$ is defined by replacing the $\gamma'(\pi)$ terms by the corresponding $B'_c(\pi, z)$ terms in (8).

A quantity, ξ, used later in the calculations, is also defined as

$$\xi = \frac{\sigma_a(z)}{B_c(\pi, z)}. \tag{9}$$

The zenith infrared radiance L_s measured at the ground can be written

$$L_s = L_{\text{sky}} + \tau L_c, \tag{10}$$

where L_c is the vertical radiance from the cloud, at cloud base, and τ and L_{sky} are respectively the transmittance and radiance of the clear atmospheric column below the cloud, due mainly to water vapor. As in P6, it is assumed

that all the atmospheric water vapor resides below the cirrus cloud. The absorption emittance ε_a is retrieved from the absorption radiance L_a,

$$L_a = L_c - L_{sc} - L_r. \quad (11)$$

The scattering components L_{sc} and L_r and their magnitudes are calculated in detail in Platt and Stephens (1980) and are also described in P1, P4, P5, and P6.

The cloud emittance ε_a is calculated by comparing the observed radiance L_a with a theoretical radiance L_{at} obtained from an equation of radiative transfer,

$$L_{at} = \int_{z_b}^{z_t} \sigma_a(z) L_B(z) \exp\left[-\int_{z_b}^{z} \sigma_a(z')\, dz'\right] dz, \quad (12)$$

where $L_B(z)$ is the filter blackbody radiance at air temperature.

b. Absorption and emission by water vapor and other trace gases

Radiant emission and absorption by water vapor are the major components of the downcoming clear-sky radiance and transmittance in the atmospheric window at the radiometer wavelengths. There is also minor absorption by other gases (P5).

For the equatorial conditions at Kavieng a model of the water vapor emission and transmittance similar to that in P5 was used. The strong continuum absorption by water vapor at the radiometer filter wavelengths is still of uncertain origin. In P5, the continuum absorption was considered to be due to the water vapor dimer and to the wings of strong lines. In a tropical atmosphere the water vapor dimer absorption accounted for over 85% of the total absorption. More recently, Clough et al. (1989) have described the continuum absorption successfully in terms of a water vapor self-broadening mechanism. Here, we assume a dimer formulation, to compare the results with our past work.

Following Lee (1973), the dimer absorption coefficient k_1 (g^{-1} cm^2) can be written as

$$k_1 = \frac{k_d e}{1000} \exp\left[-1745\left(\frac{1}{296} - \frac{1}{T}\right)\right], \quad (13)$$

where e is the water vapor pressure (in mb), T is the absolute temperature, and k_d is the absorption coefficient at 1000-mb vapor pressure and a temperature of 296 K. The formulas and values for the absorption coefficients of the weak water vapor lines and of the wings of the foreign broadened strong lines are given in P5.

4. Calibration of the data

a. Lidar data

The lidar signal voltages were first corrected for the different optical settings and for the output energy of the laser. Each lidar profile was calibrated by performing a linear regression of the measured signal to a theoretical molecular backscatter profile that was calculated from the radiosonde data (Young 1995). The altitude interval over which this fit was performed (1–5 km in depth) was determined by the inferred absence of aerosols in the region and the signal to noise ratio in the data. Because of the presence of the strong Mt. Pinatubo stratospheric aerosol layer above the clouds and because there was no aerological data above 20 km, a calibration just below cloud base was performed. When necessary, the measured lidar signal was fitted to an average reference profile above cloud top that contained the Mt. Pinatubo backscatter, assuming that this remained sensibly constant over the observational period.

Previous LIRAD studies utilized a single calibration factor for one day's run. The above new procedure allowed for any variable attenuation between the calibration altitude and the ground and for any drifts in the gain of the system.

Calibration errors were due mainly to the presence of aerosol backscatter in the calibration region. A mean standard deviation in the calibration constant of 14% for one observation period was estimated, but with variations of 1%–24% between different observation periods.

b. Infrared data

The theory of radiometer detection is given in appendix A. The radiance is calibrated by measuring the signal from an external blackbody with a variable temperature. The effective reference blackbody radiance L_{Be} [see (A4)] is checked before and after an experiment by obtaining the measured radiance for zero output voltage—a null point. The radiometer is then calibrated against a second temperature during the experiment. For the PROBE, the ARM radiometer was calibrated against liquid nitrogen and the CSIRO Mark II radiometer (in the absence of liquid nitrogen) was calibrated against an ice–water mixture.

The Mark II radiometer was pointed at the calibration blackbody by swiveling the instrument around to point downward. The ARM radiometer viewed either the calibration blackbody or the zenith sky through a gold-plated 45° scanning mirror. Corrections for the nonblackness of the calibration blackbodies and the finite emittance (ε_m) of the scanning mirror are given in appendix A.

The ARM radiometer was compared with the NOAA/ETL radiometer on two days. The ETL radiances were obtained by integrating the emission spectra over the ARM radiometer filter functions (Shaw et al. 1995). Data from the two instruments are shown in Figs. 1a and 1b. Retrieved radiances from the two instruments agreed to within 3%. Thus, the ARM radiometer calibration was assumed to be accurate.

The Mark II radiometer was operated outside the Sea-

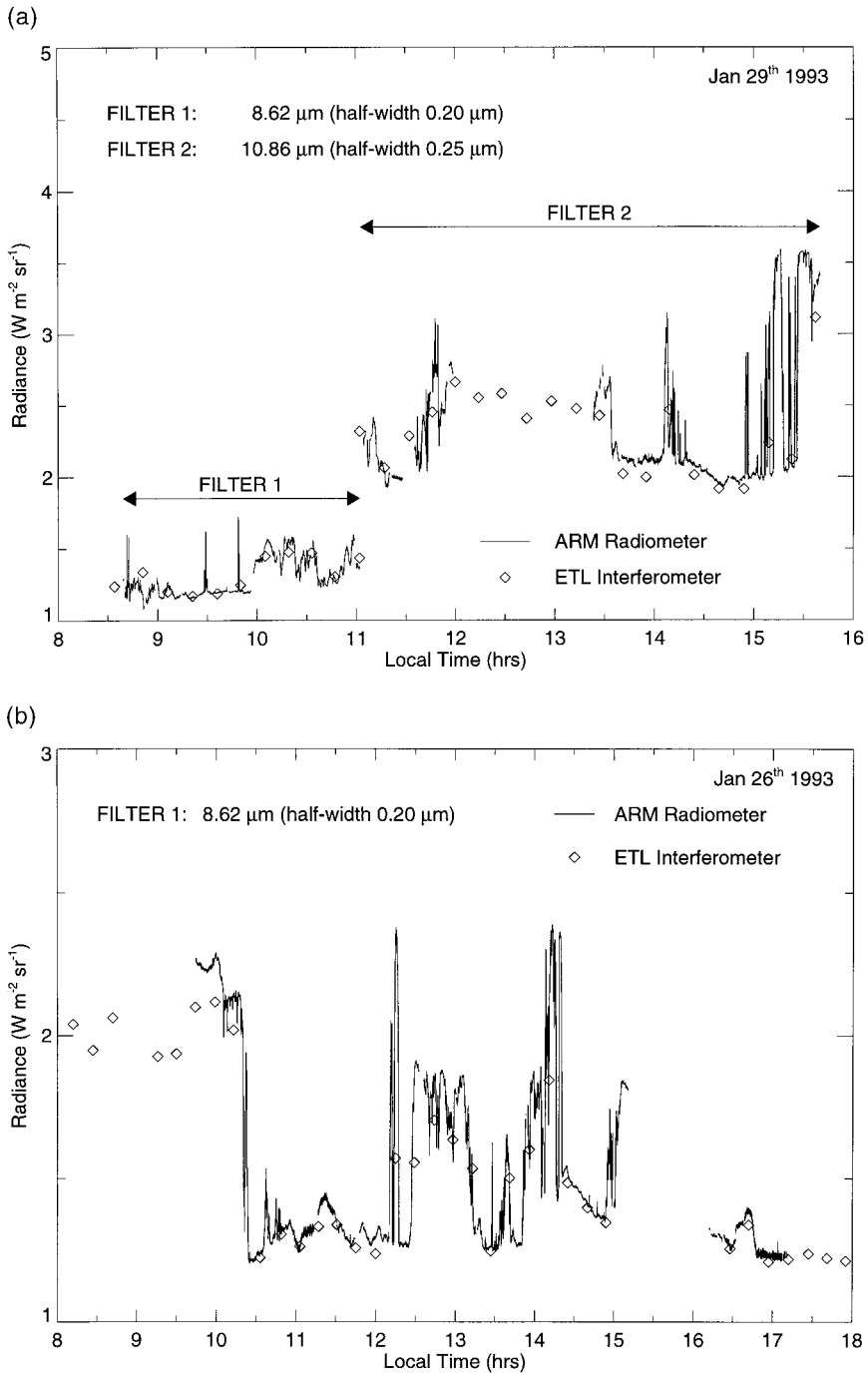

FIG. 1. Radiance from the zenith sky measured by the CSIRO ARM radiometer through two bandpass filters at 8.62 ± 0.2 μm and 10.86 ± 0.25 μm (a) on 29 January 1993. Also shown are values obtained with the NOAA/ETL interferometer; see text. (b) As in (a) but for the 8.62 ± 0.2-μm filter on 26 January 1993.

tainer, causing problems with direct sunlight and air currents on the instrument. These degraded the signal to noise ratio of the radiometer output signal. The radiometer optics also became misaligned during transport to the site. Errors caused by the above factors are described in appendices A and B.

The calibration factor S of each radiometer (A6) was measured at hourly intervals. In the case of the Mark

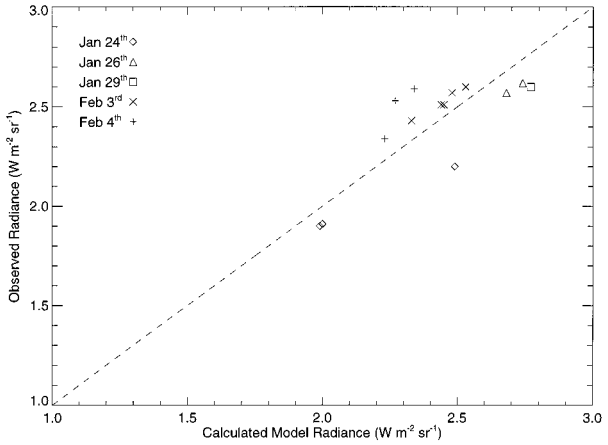

FIG. 2. Observed vertical radiance from a cloudless sky using the CSIRO Mark II radiometer (wavelength 10.84 ± 0.5 μm) plotted against radiance calculated from radiosonde data. The continuum absorption coefficient giving best fit was 9.0 ± 0.5 g^{-1} cm^2 atm^{-1}.

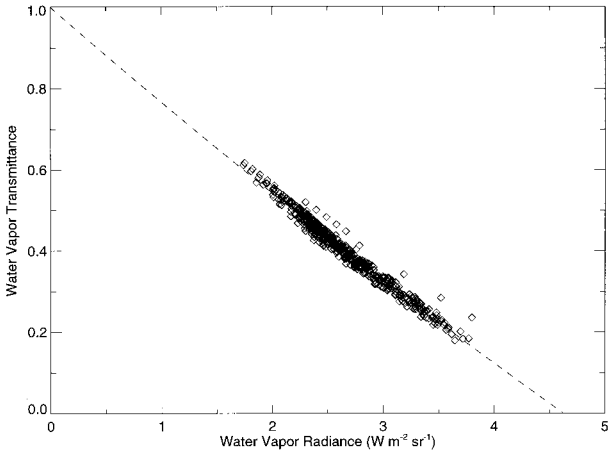

FIG. 3. Clear-sky transmittance plotted against corresponding radiance computed from radiosonde data and using a range of continuum absorption coefficients. Dashed line: see (15).

II radiometer, values of S were calculated using the effective radiance L_{Be}. The linearity of the radiometers, over the dynamic range of signal amplitudes encountered, was also checked.

5. Calculation of optical quantities

a. Clear column radiance and transmittance

As discussed earlier, the water vapor continuum effects needed to be calculated accurately. From (10), the cloud radiance can be written

$$L_c = \frac{L_s - L_{\text{sky}}}{\tau}. \tag{14}$$

At Kavieng, the cirrus was often sufficiently broken so that the radiance L_{sky} could be obtained from a value of L_s under cloudless conditions. The transmittance τ was then obtained from an equation of radiative transfer (e.g., P5; P6). The procedure was to compute the water vapor radiance for a number of dimer absorption coefficients in (13) and to vary the value of k_d until agreement with the measured value was obtained. This allowed also for any small changes in aerosol absorption. A plot of observed values of clear-sky radiance against calculated modeled values obtained from the above procedure is shown in Fig. 2. The optimum value of dimer absorption coefficient k_d in (13) for the Kavieng data was found to be 9.0 ± 0.5 g^{-1} cm^2 atm^{-1} compared to the value of 8.3 ± 0.5 g^{-1} cm^2 atm^{-1} found in P5 at Darwin. The Kavieng value is also comparable with values of 8.7 g^{-1} cm^2 atm^{-1} determined by Burch (1970), a similar figure by Lee (1973), 8.1 g^{-1} cm^2 atm^{-1} by Roberts et al. (1976), and a value of 9.6 g^{-1} cm^2 atm^{-1} determined by Bignell (1970). Clough et al. (1989) used values close to those of Roberts et al. (1976) in their LOWTRAN code to compare with observations. Westwater et al. (1995), using their interferometer in PROBE (see section 2), found that the radiance at the CSIRO radiometer wavelength of 10.84 μm (10.86 μm for the ARM radiometer) was in excess of the LOWTRAN value by about 8%. This would increase the Roberts et al. (1976) value to 8.8 g^{-1} cm^2 atm^{-1}, in reasonable agreement with the value obtained in the present study. This was expected, from the close agreement between the ARM radiometer and ETL interferometer shown in Figs. 1a and 1b.

Values of water vapor radiance and transmittance calculated for Kavieng are plotted in Fig. 3 for a range of dimer coefficients and for the radiosonde data taken over the observation period. A tight relationship is found, in agreement with Young (1984) and P5. The data were fitted by a quadratic of the form

$$\tau = 1.0 - 0.239L_{\text{sky}} + 0.00492L_{\text{sky}}^2. \tag{15}$$

Values of L_{sky} and τ at Kavieng were found to have extreme values of 3.8 W m^{-2} sr^{-1} and 0.19 respectively, compared to values at Darwin of 2.5 W m^{-2} sr^{-1} and 0.47 (P5). Thus, the water vapor corrections at Kavieng were larger than at Darwin. However, at Kavieng, continuous values of the total water vapor path measured by the microwave radiometer were also available. Values of the water vapor path and the observed zenith sky radiance for one period of observation are shown in Fig. 4. Evidently the variations in water path are of the same order as the radiance from cold cirrus at the surface. The measured water path data were thus utilized to remove the terms L_{sky} and τ in (14) on a continuous basis. Using either theoretical or measured values, the cloudless sky radiance was normalized to the water path at times of the radiosonde ascents. The radiances (and thus transmittance) at intermediate times could then be interpolated. A typical episode is shown in Fig. 5 for one period included in Fig. 4. The retrieved cirrus radiance $L_c\tau$ is also shown.

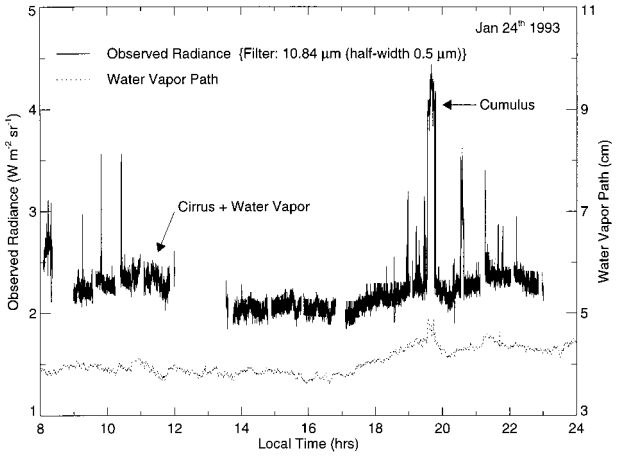

FIG. 4. Observed vertical radiance from a cloudy sky using the CSIRO Mark II radiometer (10.84 ± 0.5 μm) and water vapor path from the NOAA/ETL microwave radiometer, plotted against local time, 24 January 1993. The periodic passage of small cumulus clouds across the zenith is apparent.

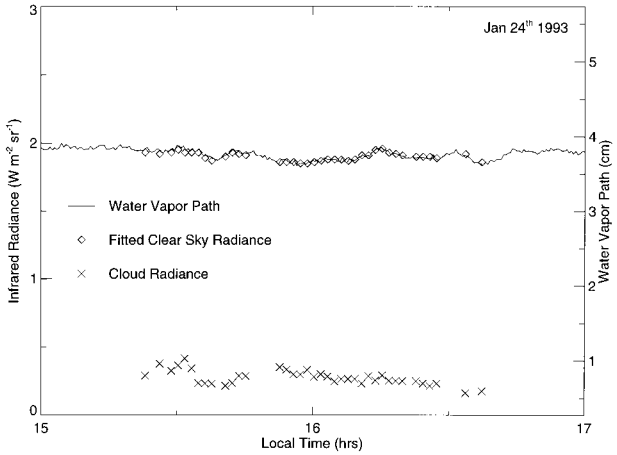

FIG. 5. Observed water vapor path, fitted clear-sky atmospheric radiance, and retrieved cloud radiance (uncorrected for atmospheric transmittance) for one period covered by Fig. 4.

b. *Cloud infrared emittance and absorption coefficient (10.84 μm)*

The calculated value of L_c was first corrected for the cloud scattering components in (11). Absorption coefficients at different levels in the cloud were then calculated using (12) together with a profile of cloud backscatter coefficient $B_c(\pi, z)$ (see section 5c). Initial values of σ_a were calculated by using a trial value of ξ in (12) [see (9)]. A value of L_{at} was then calculated and the value of ξ adjusted until L_{at} equaled the measured value, L_a. Blackbody radiances $L_B(z)$ in (12) were obtained from atmospheric temperatures interpolated linearly both in height and time between the 6-hourly radiosonde data.

The infrared emittance ε_a was then calculated from (4) and (5). Values of ξ were found to vary appreciably between cloud profiles. Apart from errors of measurement, these variations were assumed to be due to changes in cloud ice particle size distribution and ice crystal habit.

c. *Cloud backscatter coefficient (0.532 μm)*

Values of $B_c(\pi, z)$ were retrieved by rearranging (2) to give

$$B_c(\pi, z) = \frac{B'(\pi, z)}{\tau_m^2 \tau_c^2} - B_m(\pi, z), \tag{16}$$

where

$$\tau_m^2 = \exp\left[-\int_{z_b}^{z} 2\sigma_m(z')\, dz'\right] \tag{17}$$

and

$$\tau_c^2 = \exp\left[-\int_{z_b}^{z} 2\eta(z')\sigma_c(z')\, dz'\right]. \tag{18}$$

At each altitude step z in the retrieval process an initial estimate of $B_c(\pi, z)$ was calculated from (16) using the substitution

$$\eta(z)\sigma_c(z) = \frac{\eta(z)B_c'(\pi, z)}{k} \tag{19}$$

in (18). By substituting successive estimates of $B_c(\pi, z)$ in (19), the values of $B_c(\pi, z)$ in (16) could be obtained to the desired accuracy (P1). The quantity $k/2\eta$ was obtained from the value of $\gamma'(\pi)$ when ε_a tended to unity. If this did not occur, then values of $k/2\eta$ were obtained from adjacent results. Values of the molecular backscatter $B_m(\pi, z)$ and extinction $\sigma_m(z)$ were calculated from atmospheric temperature and pressure (altitude) values interpolated between successive radiosonde flights.

If the cloud optical depth exceeds a certain amount below some level z, then the solution can lead to successive values of $B_c(\pi, z)$ that diverge. This effect can be halted by increasing the value of $k/2\eta$ in small increments (5% in this study) until convergence is again achieved (P1). The value of the cloud optical depth will then be in error by an amount dependent on both the optical depth and the increment in $k/2\eta$ (P1) (see appendix B). By replotting values of $\gamma'(\pi)$ against ε_a, more accurate values of $k/2\eta$, and thus $B_c(\pi, z)$ and ε_a, can then be obtained.

Figures 6a and 6b show normalized profiles of the total (i.e., molecular plus cloud) attenuated backscatter signal. Molecular backscatter is obviously quite significant in Fig. 6a but much less so in Fig. 6b. The attenuated backscatter from the Mt. Pinatubo volcanic aerosol veil is very evident in Fig. 6a (see section 4a).

Values of cloud base z_b and top z_t were retrieved using the standard deviation method described by Young (1995), together with visual inspection to check for false detection caused by noise in the data.

The cloud visible optical depth δ_c was calculated from

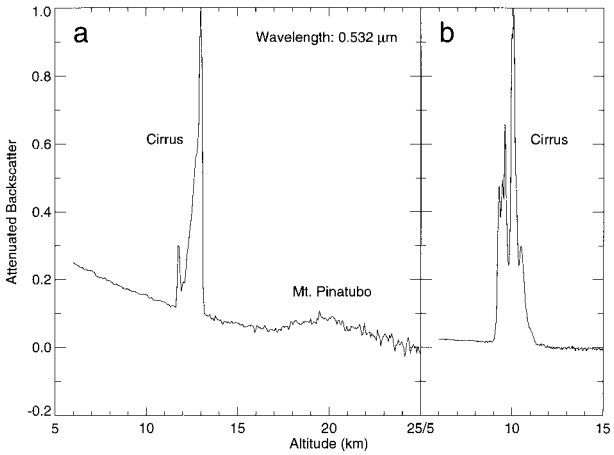

FIG. 6. Lidar-derived attenuated backscatter profile for two cases normalized to unity at peak signal. (a) Weak cirrus return showing molecular and aerosol returns below and above the cloud; peak value of backscatter coefficient = 3.6×10^{-5} m^{-1}. (b) Strong cirrus return. Peak value of backscatter coefficient = 3.77×10^{-4} m^{-1}.

(4) with $\sigma_a(z)$ replaced by $\sigma_c(z)$. Values of $\sigma_c(z)$ were calculated from (19) employing the final retrieved value of $B_c(\pi, z)$.

6. Results

a. Cloud depth and height

The distribution of cloud depth with midcloud temperature is shown in Fig. 7. The bars show the standard deviation in cloud depth between profiles. The accuracy of measurement of cloud boundaries is estimated as 30 m for cloud base and 50 m for cloud top so that most of the standard deviation represents the variability in cloud depth. The lidar pulse *invariably* reached cloud top before complete attenuation occurred.

The clouds at Kavieng were about twice as deep, on

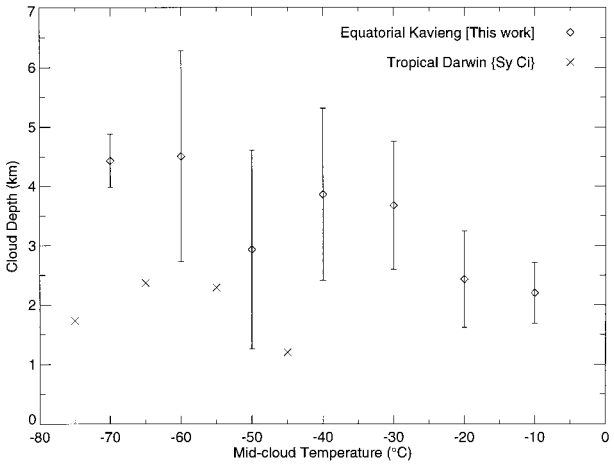

FIG. 7. Average and standard deviation of measured cloud depth in 10°C temperature intervals plotted against midcloud temperature. Tropical Darwin synoptic cirrus data are from P6.

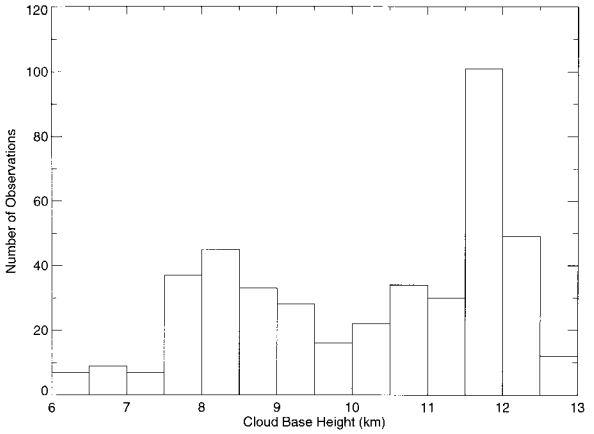

FIG. 8. Number of observations of cloud base height in 0.5-km intervals of cloud height.

average, than the synoptic cirrus measured at Darwin (P5). The clouds at the lower temperatures still possessed considerable thickness. The clouds were sometimes composed of several layers that were, however, never more than 1 km apart in height. For analysis purposes they were still considered to be a single entity. Such multilayered cirrus do not cause problems in the LIRAD analysis. The base (top) of the lowest (highest) layer is considered as cloud base (top). The cloud bases covered a wide range of altitudes as shown in Fig. 8.

b. Cloud infrared emittance and absorption coefficient at 10.84 μm

A frequency histogram of cloud emittance is shown in Fig. 9. The histogram is much flatter in appearance than those obtained at midlatitudes, with emittances almost equally likely between values of 0.05 and 0.85.

The emittance is plotted against midcloud temperature in Fig. 10. The bars again show the standard deviation of measured emittance. Emittances are compa-

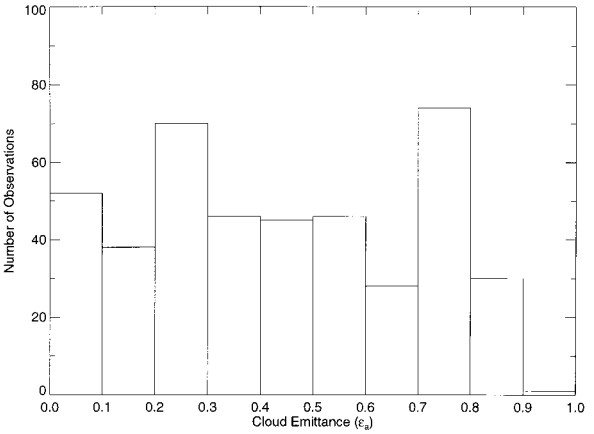

FIG. 9. Number of observations of cloud absorption emittance ε_a in 0.1 intervals of ε_a.

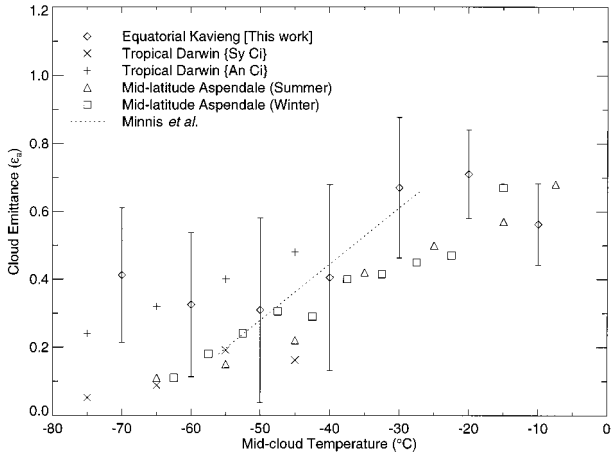

FIG. 10. Mean cloud absorption emittance ε_a in 10°C temperature intervals plotted against midcloud temperature. Data on Darwin storm anvil cirrus are from P5, on Darwin synoptic cirrus and midlatitude cirrus from P6. The dashed line is from Minnis et al. (1990).

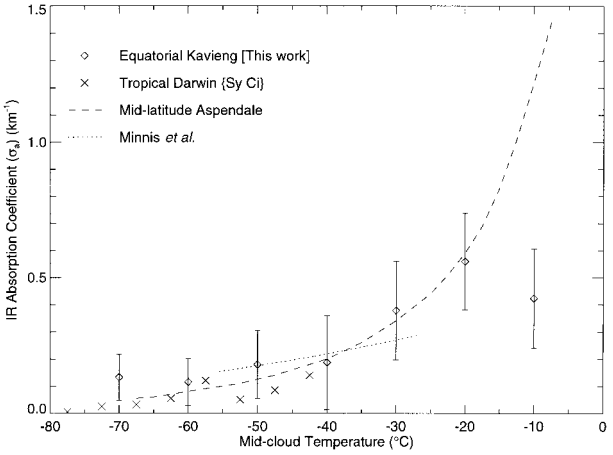

FIG. 12. Infrared absorption coefficient σ_a in 10°C temperature intervals plotted against midcloud temperature. The Darwin synoptic cirrus points and dashed line are from P6. Dotted line is from Minnis et al. (1990).

rable with the Darwin anvil values (P5) but are higher than the synoptic values (P6), particularly at the lower temperatures. As mentioned previously, none of the cirrus clouds sampled at Kavieng had any association with local storm anvils. A frequency histogram of cloud optical depth δ_a obtained from (4) is shown in Fig. 11. The higher values of optical depth occurred mainly in large cirrus uncinus cells on 3 and 4 February. None of the measured cirrus emittances approached unity, so optical depths could always be calculated with reasonable accuracy.

The mean infrared absorption coefficient σ_a plotted against temperature is shown in Fig. 12. Values of σ_a were obtained by dividing the optical depth δ_a by the cloud thickness, $z_t - z_b$. Values are seen to increase with temperature in a similar manner to the midlatitude values except at the highest temperature. The values of Minnis et al. (1990) are also comparable.

c. Cloud visible optical depth

A frequency histogram of cloud visible optical depth calculated for each cloud profile is shown in Fig. 13. Here δ_c varies from very low values to a maximum value of 9. This value is greater than the maximum value of δ_a because the value of α in (6) varies between 1.77 and 5.26 (see Table 3). The high values of optical depth can be retrieved because the low values of η at cirrus ranges effectively reduce the optical depth to $\eta\delta_c$. However, values of δ_c greater than 6 should be treated with caution because of the considerable errors in retrieval at these high values (see appendix section Bb and P1).

d. Dependence of lidar integrated backscatter on infrared emittance

Plots of the integrated backscatter $\gamma'(\pi)$ versus infrared emittance ε_a are shown in Figs. 14a and 14b for

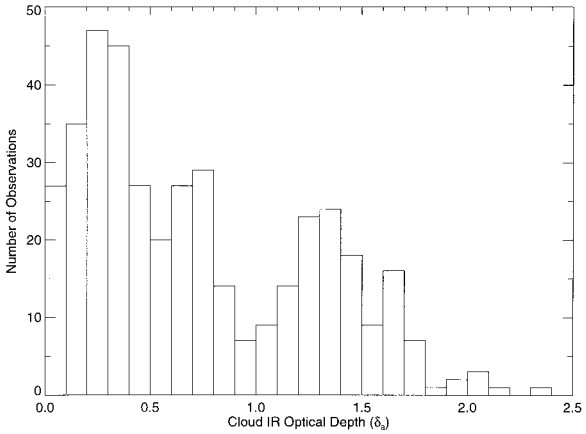

FIG. 11. Number of observations of infrared absorption optical depth δ_a in 0.1 intervals of δ_a.

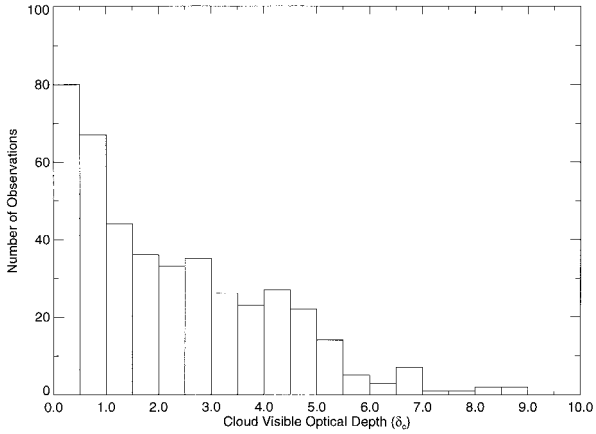

FIG. 13. Number of observations of visible optical depth δ_c in 0.5 intervals of δ_c.

TABLE 3. Derived values of $k/2\eta$, k, $2\alpha\eta$, and α (uncertainties shown in parentheses). The linear equation of fit giving $k/2\eta$ in terms of T is $k/2\eta = 3.43 \times 10^{-3} \times T + 3.91 \times 10^{-1}$.

Temperature interval (°C)	$k/2\eta$	η*	k*	$2\alpha\eta$	α*
−75 to −65	0.14 (0.02)	0.30 (0.07)	0.08 (0.03)	2.9 (0.46)	4.83 (2.00)
−65 to −55	0.18 (0.04)	0.36 (0.08)	0.13 (0.05)	3.8 (0.57)	5.26 (1.90)
−55 to −45	0.22 (0.05)	0.42 (0.08)	0.18 (0.07)	3.6 (0.47)	4.29 (1.40)
−45 to −35	0.29 (0.04)	0.48 (0.08)	0.28 (0.08)	1.7 (0.20)	1.77 (0.51)
−35 to −25	0.29 (0.04)	0.54 (0.09)	0.31 (0.09)	2.4 (0.19)	2.22 (0.55)
−25 to −15	0.30 (0.06)	0.60 (0.10)	0.36 (0.10)	3.2 (0.16)	2.67 (0.80)

* The multiple scattering factor used to calculate k and α is $\eta = 0.72 + 6 \times 10^{-3} \times T$ (T in °C).

one higher and one lower cloud temperature. The values in two intervals covering the total temperature range are shown in Figs. 15a and 15b. Curves of the function given by (7) were fitted to the data in the various temperature ranges studied. Values of $k/2\eta$ obtained from these curves and plotted against midcloud temperature are shown in Fig. 16, where they are compared with values from P5 and P6. The values are seen to increase steadily with temperature and are comparable with the summer Aspendale values. Values below −55°C are considerably lower than those observed at Darwin. A

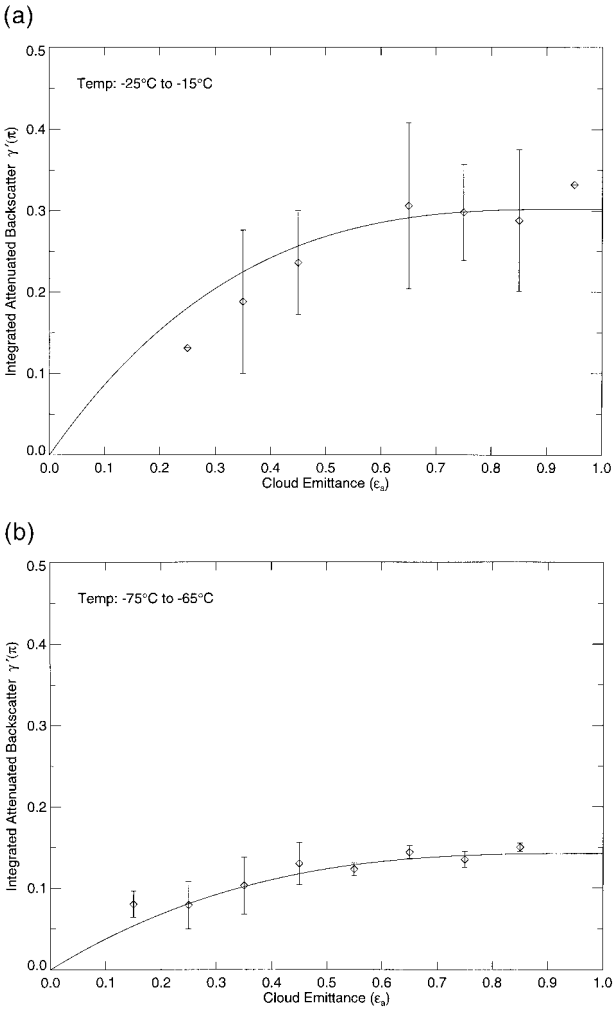

FIG. 14. Mean integrated attenuated lidar backscatter $\gamma'(\pi)$ plotted against cloud absorption emittance ε_a (10.84 μm) in intervals of 0.1 for (a) temperature interval of −25° to −15°C. Full line is from (7) with $2\alpha\eta = 3.2$, $k/2\eta = 0.3$. (b) As in (a) but for temperature interval of −75° to −65°C: $2\alpha\eta = 2.9$, $k/2\eta = 0.14$.

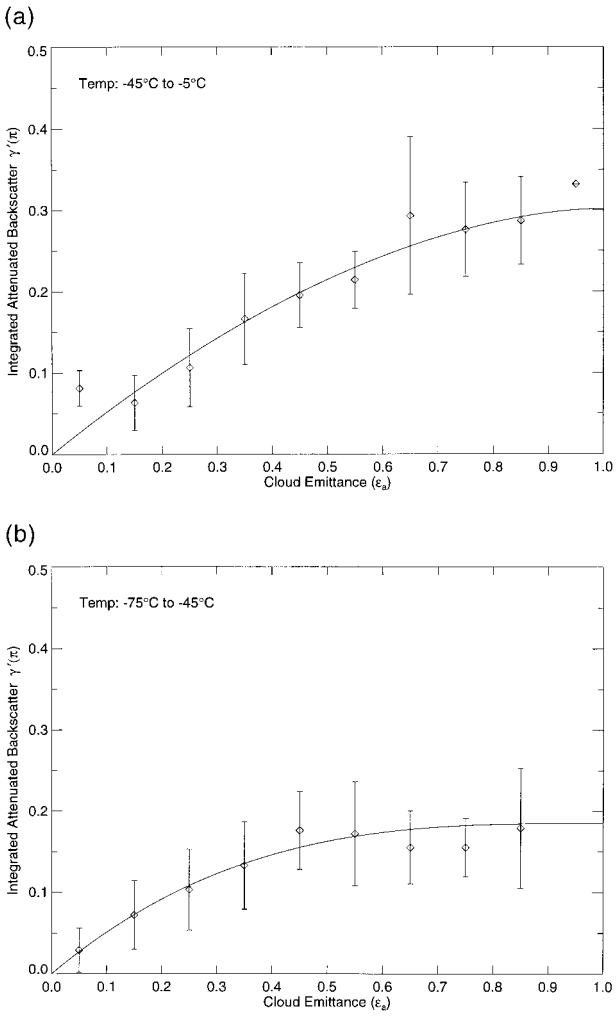

FIG. 15. As in Fig. 14 but (a) for temperature interval of −45° to −5°C: $2\alpha\eta = 1.8$, $k/2\eta = 0.3$ and (b) for temperature interval of −75° to −45°C: $2\alpha\eta = 3.1$, $k/2\eta = 0.18$.

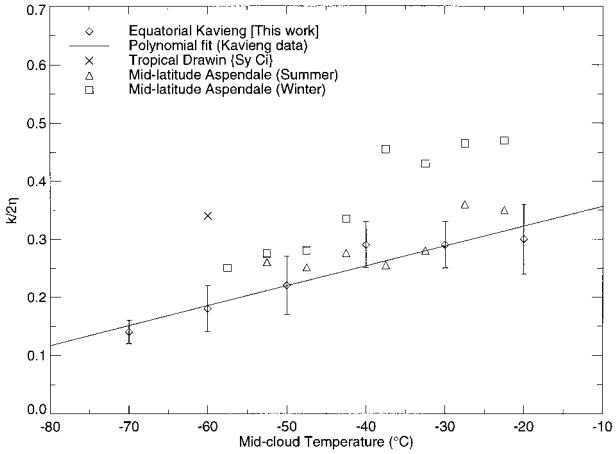

FIG. 16. Mean cloud isotropic backscatter to extinction ratio $k/2\eta$ in 10°C temperature intervals plotted against midcloud temperature. Tropical Darwin data and midlatitude Aspendale data are from P6. The full line is a linear fit to the Kavieng data (see Table 3).

linear fit to the Kavieng values of $k/2\eta$ was utilized in the retrieval of backscatter coefficient (section 5c). The equation of the fitted line, together with values of $k/2\eta$ and $2\alpha\eta$ and derived values of k and α, are listed in Table 3. The latter were calculated from an approximate expression for η also shown in Table 3. This expression was based on data calculated by Platt (1981, hereafter referred to as P3).

e. Depolarization ratio and cloud phase

The cloud linear depolarization ratio $\Delta(z)$ was measured during some selected periods of observation. Values of $B'_c(\pi, z)$ and $\Delta(z)$ are shown in Figs. 17a and 17b for a cirrus cloud on 3 February. Representative temperature and humidity profiles, and the relative humidity at ice saturation, are shown in Fig. 17c. The low values of $\Delta(z)$ and the high backscatter near cloud base suggest the presence of either supercooled drops or horizontal ice crystal plates (Platt 1978). The profile of humidity in Fig. 17c, indicating values below ice saturation, suggests the latter. However, the humidity data may have systematic errors, so conclusions are only tentative. Figure 18 shows the lidar profiles at one time in the period depicted in Fig. 17 and illustrates again the high backscatter in one region of low depolarization. However, backscatter coefficients were nowhere near as high as measured in Platt (1978). The value of integrated backscatter for Fig. 18 was only 0.37, much less than usually observed for horizontal plate backscatter and more typical of that from water drops. The detection threshold of the microwave radiometer would have been greater than likely water path values so that these would not have been detected. The higher values of $\Delta(z)$ near the cloud-top boundaries are an artifact due to the low noisy values of backscatter in those regions. Figure 19 shows a summary of values of integrated depolarization ratio Δ [see (8)] and their dependencies on temperature, showing a systematic decrease of Δ with temperature. This tendency is similar to that obtained in midlatitude clouds (P6), as shown by the broken lines. The values at Kavieng were somewhat lower for temperatures less than about −30°C. The high values of $\Delta(z)$ near the cloud boundaries in Figs. 17b and 18 will not affect the values of Δ as the latter are the ratios of two *integrated* values [see (8)].

7. Discussion

The water vapor paths measured by the NOAA/ETL microwave radiometer shown in Figs. 4 and 5, together with the water vapor and cloud radiances, indicate the magnitude of the corrections to be made to obtain the cloud radiances. Thus, the presence of water vapor increases the uncertainty in the retrieval of the emittances of the colder clouds quite considerably (see sections 5a and 5b and appendix B).

It should be reiterated here that *none* of the cirrus clouds observed were associated directly with storm anvils. The most favorable periods of continuous cloud observations occurred when convective cloud amounts were small, or intermittent. Some of the cirrus cells appeared to thicken during the morning and early afternoon but dissipate again toward evening.

The large cloud depths shown in Table 2 and Fig. 7 indicate the great depths of moist air that were often observed in the equatorial upper troposphere. As indicated by the radiosonde data in Fig. 17c, the height distribution of humidity was quite layered. The clouds, as shown in Fig. 17a, sometimes showed the same layering characteristics. The measured humidity remained fairly close to ice saturation throughout the upper troposphere, although systematic errors could be present. The troposphere at Kavieng was perhaps slightly deeper compared to that over Darwin. The Darwin synoptic clouds tended to be connected more with midlatitude disturbances, whereas the equatorial cirrus tended to be associated more with deep moist layers. As shown in Fig. 9, higher emittance clouds were more frequent in the equatorial regions than at midlatitudes (P4; P6). However, the highest emittance recorded at Kavieng was only 0.91.

In the temperature representation of Fig. 10, values of ε_a were larger for clouds colder than about −20°C compared to midlatitude clouds. Minnis et al. (1990) found a rather similar dependence of emittance with temperature, as also shown in Fig. 10.

The histogram shown in Fig. 11 indicates that infrared optical depths between 1 and 2 occur about 30% of the time but that optical depths over 2 represent only 2% of the sample. Values of infrared absorption coefficient σ_a shown in Fig. 12 are very similar to those found at midlatitudes (P6) but slightly higher than those found at Darwin. The higher values of emittance in the equatorial case are thus likely to be due to the deeper clouds.

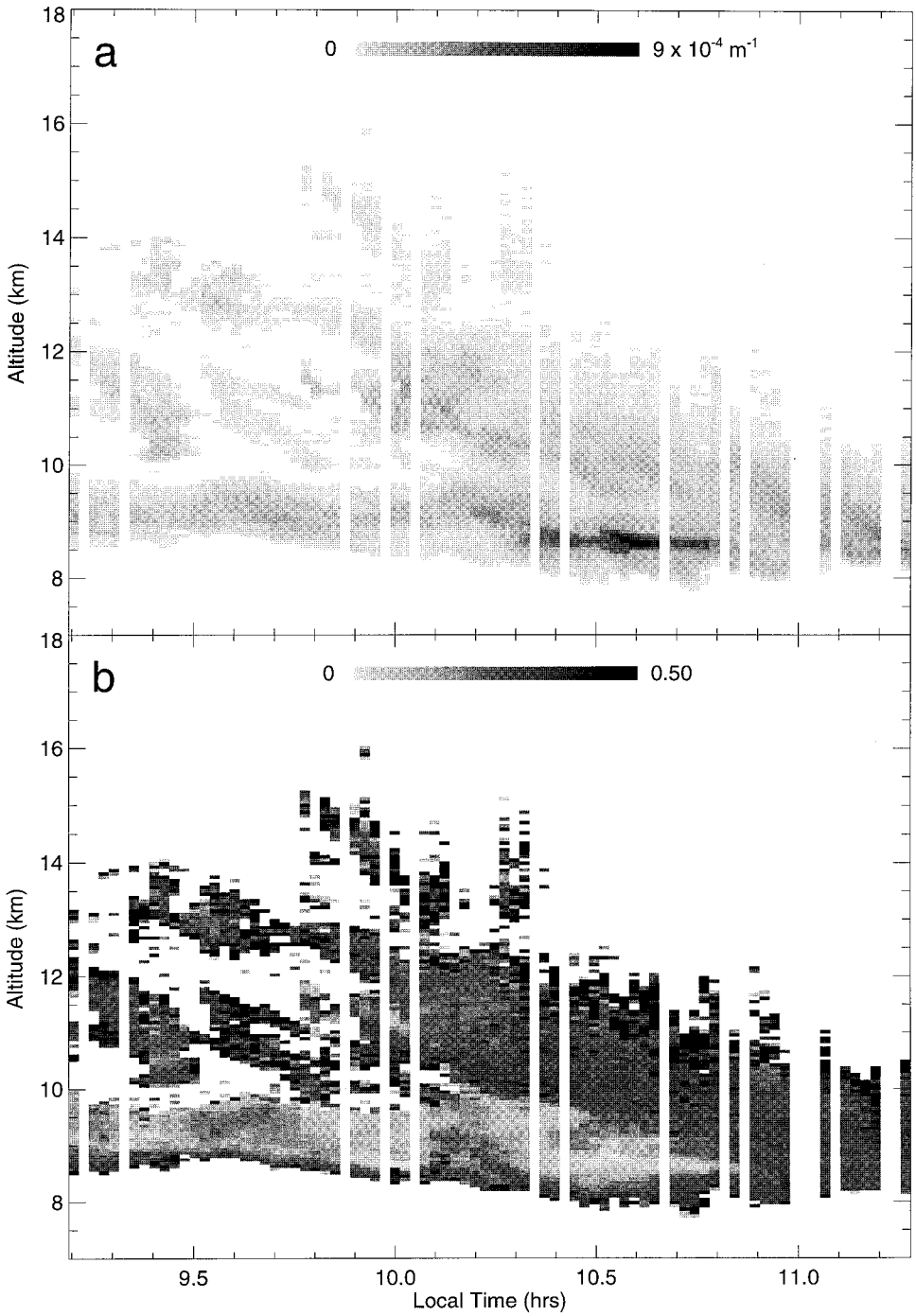

FIG. 17. Time–height representations of (a) cloud attenuated backscatter coefficient, $B'(\pi, z)$; (b) cloud linear depolarization ratio, $\Delta(z)$; (c) temperature and relative humidity profiles and profile for ice saturation, 0900 LT 3 February 1993. High values of $\Delta(z)$ near cloud boundaries are due to weak signals.

The continuous falloff in frequency of visible optical depth shown in Fig. 13 agrees with the results found in midlatitude clouds by Pal et al. (1995). However, as emphasized previously, values of optical depth greater than about 6 can be considerably in error (see also appendix B).

The plots of integrated backscatter $\gamma'(\pi)$ versus ε_a shown in Figs. 14 and 15 are typical of those obtained previously from cirrus clouds (e.g., P6). The deduced values of $k/2\eta$ shown in Fig. 16 indicate a nearly monotonic increase with temperature very similar to the midlatitude summer values, although absolute values are

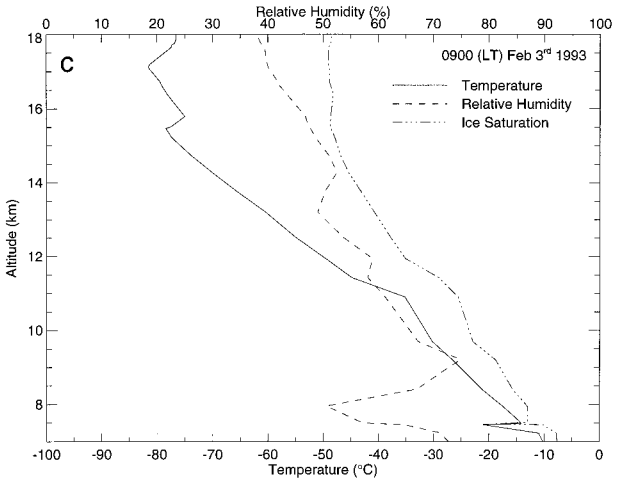

FIG. 17. (*Continued*)

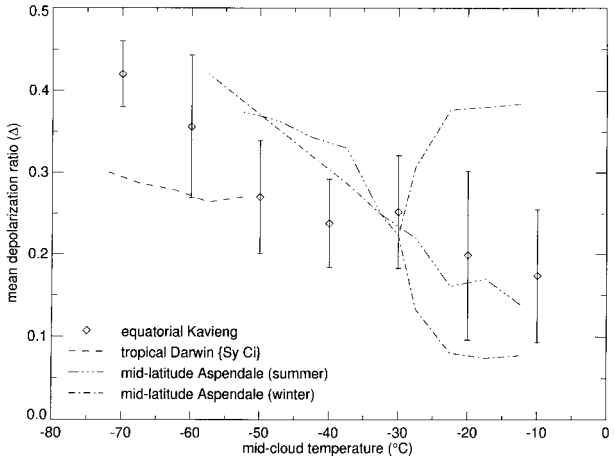

FIG. 19. Cloud integrated lidar depolarization ratio Δ for all profiles in each 10°C temperature interval plotted against midcloud temperature. Tropical Darwin and midlatitude Aspendale data are from P6.

slightly lower. Values are also much lower than the midlatitude winter values, especially in the −40° to −20°C temperature region. At the higher temperatures, values may be affected by backscatter from horizontal ice crystal plates (section 6e). The Darwin tropical values remained rather similar over the temperature ranges considered in P5 and are thus plotted as a single point. The approximate expression in Table 3, giving η as a function of midcloud temperature T, gives the expected increase of η with T (i.e., decrease of η with cloud height, as given in P3). This increase reinforces the rate of change of k with T over that of $k/2\eta$. It might be expected that η should increase with altitude as the cloud particles tend to become smaller. However, the reverse occurs because of the strong decrease in η with both range and with decreasing optical depth (P3).

Experimental values of k reported by other authors show a wider spread in values than those observed at Kavieng. For example, Sassen et al. (1990) measured values of 0.29 at −51°C and 0.25 at −48°C, values closer to those found at Darwin. Spinhirne and Hart (1990) found values equal to 0.16 at −48°C and 0.127 at −40°C, and Platt et al. (1989) found values of 0.27 at −62.7°C and 0.18 at −47.3°C. Ansmann et al. (1992) were able to measure *variations* in k through the cloud depth, using the addition of a nitrogen Raman lidar channel. Their values of k varied from 0.7 to over 2. Values reported by Sassen and Cho (1992) for thin cirrus showed considerable scatter but with a tendency for an increase in values with temperature. Their values varied between 0.025, for very thin ''invisible'' cirrus, and 0.69.

Theoretical values of k are shown in Table 4. The derived PROBE values increase to higher values than those given by Macke (1993) but otherwise the values seem to span approximately the same ranges. Values given by Takano and Liou (1995) exhibit a larger range, as well as higher values for solid columns and bullet rosettes. However, their values for hollow columns are close to those reported by Macke (1993). Recently, Yang and Liou (1996), using a new method of computation for small crystal sizes, calculated values of k considerably lower than those calculated by geometric optical ray-tracing methods. For a solid column of length 11 μm, wavelength of 0.55 μm, and length-to-width ratio

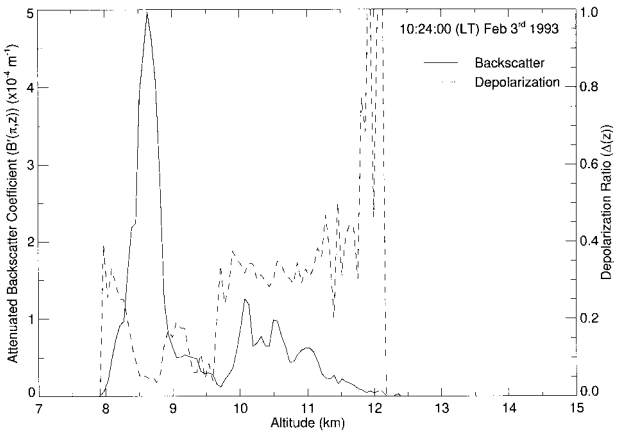

FIG. 18. Cloud attenuated backscatter coefficient (full line) and linear depolarization ratio, Δ(z), (dashed line) vs altitude, 1024 LT 3 February 1993.

TABLE 4. Some values of backscatter to extinction ratio k calculated from scattering theory.

	Backscatter to extinction ratio k	
Crystal habit	Macke (1993)	Takano and Liou (1995)
Solid bullet	0.10	
Hollow column	0.11	0.08–0.10
Bullet rosette	0.11	0.33–0.51
Solid column	0.16	0.90
Capped column	0.22	

(L/d) of 3, k was found to be 0.03 but increasing to 0.25 for an L/d of 1. For a hollow column with an L/d of 3, the k value dropped to 0.012. For a bullet rosette of equivalent length, the value of k was 0.20. Irrespective of crystal habit, the lower values calculated for the smaller crystals would indicate that the observed crystals at Kavieng were smaller at the lower temperatures. On the other hand, the observed change in k with temperature could, from Macke's values, indicate that there were more hollow columns at the lower temperatures. However, it could also indicate that there were still hexagonal columns, but of smaller size.

In the above interpretations, the effects of gravity must also be considered. All crystals will fall under gravity, the larger crystals falling at the highest speeds. Thus, crystals will be measured at different levels to where they were first formed. Any measured temperature dependencies of crystal size or habit will thus become blurred. Nevertheless, the distinct change found in mean crystal size with temperature and thus altitude (e.g., Heymsfield and Platt 1984; Platt 1997) indicates that substantial temperature dependencies are preserved.

The values of $2\alpha\eta$ shown in Table 3 exhibit considerable scatter, due partly to the uncertainties shown in Table B2. However, a general trend in $2\alpha\eta$ to smaller values at the higher temperatures is in agreement with P6, although values appear to be generally higher in the present work. Derived values of α are also shown in Table 3 together with the total estimated errors. Very high values at the lower temperatures are apparent. Such values are difficult to reconcile with a model of ice cylinders (P1) where the value of α is only 3 for a cylinder radius of 5 μm. However, work done recently by Mitchell and Arnott (1994) and D. L. Mitchell (1996, personal communication) with a modified theory of scattering by ice crystals gives lower infrared absorption coefficients for ice crystals compared to ice cylinders of equivalent radius. For bullet rosettes, Mitchell's curves give a value of α equal to 4 for a mean dimension of 7 μm. Minnis et al. (1990) found values of α greater than 3 at temperatures less than -63°C. Within the quoted margins of error, the derived values of α for the lower temperatures, assuming small particles, thus appear to be realistic. The assumption of small particles is also consistent with the previous conclusions based on the lower values of k at the lower temperatures.

Observational data to support the high values of α (that is, small particles) over Kavieng are rather rare. Heymsfield and McFarquhar (1996) reported the presence of numerous small particles in equatorial cirrus during CEPEX. They also reported on some earlier data observed near Kwajalein in the Pacific that showed crystal dimensions of typically less than 10-μm length in clouds near the tropical tropopause. The crystals often had the appearance of solid columns (small) and hollow columns (large). Again, Knollenberg et al. (1993) sampled clouds near the tops of mesoscale convective systems during the Stratosphere–Troposphere Exchange Project in 1987. They recorded an abundance of small particles at temperatures of about -78°C. A calculation (assuming spheres) from one of their published spectra gives a typical mean diameter of 7 μm. Although presumably formed under different conditions from the Kwajalein clouds, such small crystals would obviously remain at high altitudes after the dissipation of the rest of the system. Finally, Wang et al. (1994) investigated the extinction and particle size distributions of tropical high clouds from the Stratospheric Aerosol and Gas Experiment (SAGE II). Wang et al. found that high tropical clouds existed for about 80%–90% of the time over the warm pool region in the Southern Hemisphere summer season. These figures are in qualitative agreement with the almost continuous occurrence of cirrus found at Kavieng during the observational period. Wang et al. (1994) were only able to deduce size distributions for particles smaller than 1 μm because of the wavelength limitations of their instrument. However, they were able to separate scatter effects between aerosols and ice particles using the ratios of the scatter at two wavelengths. All episodes labeled as clouds were found to lie in the 16.5–18.5-km altitude region with temperatures in the narrow range of $-76°$ to -73°C. The temperature range of the high values of α in the present study was much greater, covering observations from about $-75°$ to about -45°C. Nevertheless, the above observations do indicate that very small particles can occur in cirrus at low cloud temperatures.

The results indicated an increase in the integrated linear depolarization ratio Δ toward lower temperatures. This would be accentuated, for the case shown in Fig. 18, by the presence of ice crystal plates. However, supercooled water might also have been present. There are very little theoretical data to compare with the present data. Takano and Liou (1995) have recently published values of $\Delta(z)$ for solid hexagonal columns and for columns with various degrees of hollowness. They found that for a hollow hexagonal column the value of $\Delta(z)$ *decreases* as the length of the hollow inclusion *increases*, from a value of 0.55 for no inclusion to a value of 0.242 for an inclusion of length 100 μm and a crystal length of 200 μm. This behavior is opposite to what would be predicted from the behavior of the quantity k in Table 3, which would indicate that the number of hollow columns might *increase* with decreasing temperature. Thus, the values of k that require more hollow columns at the lower temperatures are not consistent, in this interpretation, with the values of Δ that require less. However, the changes could indicate the presence of smaller solid columns at the lower temperatures, which, according to Sassen and Cho (1992), would give lower values of k. This interpretation would also be in agreement with the observed increase in α as the temperature decreased.

Sassen (1992) observed low values of depolarization ratio $\Delta(z)$ at the tops of some cirrus clouds that he attributed to the formation of new droplets from volcanic

nuclei. No such low values were observed at the tops of the Kavieng clouds studied, despite the close proximity of the Mt. Pinatubo volcanic layer (Fig. 6a). Sassen and Cho (1992) recorded much higher values of $\Delta(z)$ in very thin cirrus, values that increased toward lower temperatures, in agreement with the present data. Nucleating processes at these altitudes and temperatures are complex, as discussed by Wang et al. (1994). However, without having any independent measurement of ice crystal type, it is not possible to speculate any further on the origin of the Kavieng cirrus crystal formation.

8. Summary and conclusions

The results discussed in this article represent an ongoing effort to quantify fully the optical properties of clouds at various levels in the atmosphere and at various latitudes, using the LIRAD method. Earlier results on midlatitude cirrus and tropical cirrus are given in P6. Some results on tropical cirrus anvils were given in P5. The recent Kavieng data reported here, as well as contributing to the LIRAD archive, were also obtained as initial comparison datasets for the new ARM TWP cloud and radiation testbed on Manus Island, some 300 km west-northwest of Kavieng.

The clouds studied represented a comparatively small sample, but nevertheless, some characteristics emerged that were similar to those found in past studies. The Kavieng clouds were observed to be very deep in the mean, leading to relatively high infrared emittances and infrared and visible optical depths. Both the backscatter to extinction ratio k and visible extinction to infrared absorption ratio α exhibited behavior that had similarities to previous observations. Values of k increased fairly systematically with temperature. Values of α exhibited higher values at the lower temperatures, indicating the presence of small particles. At higher temperatures, values of α were similar to what had been measured before in midlatitude cirrus. Values of infrared absorption coefficient σ_a were rather similar to those of a number of past studies, leading possibly to a useful parameterization, as well as validation, of climate models.

Values of the integrated depolarization ratio Δ increased toward lower temperatures, in qualitative agreement with other studies. This behavior may be a function of the smaller crystals at lower temperatures, although no theoretical calculations were available to confirm this. Layers of plate crystals were detected in the $-18°$ to $-25°$C temperature range.

The value of 9.0 ± 0.5 g^{-1} cm^2 atm^{-1} determined for the water vapor continuum absorption coefficient is in reasonable agreement to values determined previously.

Contrary to what might be expected, none of the cirrus observed was associated directly with local thunderstorm anvils. Such anvils tended to be obscured by middle-level and low cloud when thunderstorms were close.

In conclusion it is clear that the LIRAD method can yield detailed information on cloud optical properties and cloud microphysics. It is obviously important to make further studies on cirrus and the ambient humidity in the equatorial regions, as will be done at the ARM tropical site on Manus Island, PNG.

Acknowledgments. The PROBE field trip, the components, and part of the design and construction of the ARM Mark I radiometer and the analysis were supported by the U.S. Department of Energy, Office of Health and Environmental Research, Grant No. DE-FG02-92ER61373. Messrs. John Bennett, Reg Henry, Brian Turner, and Bernard Petraitis, of the CSIRO, Division of Atmospheric Research, designed and fabricated the ARM Mark I radiometer. The authors also acknowledge the permission and help given by the PNG Bureau of Meteorology in the use of their observation site at Kavieng.

APPENDIX A

Theory of the Radiometers

a. Theory of radiometer detection

The following discussion applies to both the CSIRO ARM and MARK II radiometers, which essentially operate in the same manner (Platt 1971). The incoming signal to the radiometer is compared with that from a chopped reference blackbody, at a controlled temperature, which comprises half of the input aperture. The radiative flux incident on the detector is restricted to wavelengths from λ_1 to λ_2 passed by the narrowband filter used. An effective blackbody radiance $L(T)$ at temperature T is thus defined as

$$L(T) = \int_{\lambda_1}^{\lambda_2} F(\lambda)B(\lambda, T)\, d\lambda, \qquad \text{(A1)}$$

where $F(\lambda)$ is the filter factor and $B(\lambda, T)$ the Planck function at a wavelength λ.

In what follows, the radiometer is assumed to be observing an external source. In the simplest case, the detector receives flux from equal areas and solid angles of the radiometer aperture and reference blackbody respectively. The output voltage v_s is given by

$$v_s = \beta(L_B - L_s), \qquad \text{(A2)}$$

where L_B and L_s are the radiances of the reference and signal sources respectively and β is a response factor. It is assumed in (A2) that the value of the reference blackbody emittance is unity and that the detector response is linear.

In practice, sections of the aperture and reference blackbody are obscured by a secondary mirror support. Also, because of small distortions in the optical system, the effective viewing solid angle may vary around the aperture. Finally, practical blackbody emittances are al-

ways less than unity. A more general expression for the detected voltage v_s is then

$$\frac{v_s}{\beta} = L_B\varepsilon_1(1-\gamma_1) - L_s(1-\gamma_2) + L_\theta(\gamma_1-\gamma_2), \quad \text{(A3)}$$

where ε_1 is now the emittance of the reference blackbody and L_θ is the blackbody radiance at ambient temperature. The factors γ_1 and γ_2 define those fractions of the fields of view of the reference blackbody and source respectively that are at ambient temperature. Now, (A3) is linear in v_s and L_s so that the latter can be determined by obtaining values of v_s at at least two temperatures. This is normally done with an external blackbody by varying the blackbody temperature to obtain a null condition ($v_s = 0$). Then, from (A3),

$$L_s(v_s = 0) = \frac{L_B\varepsilon_1 f}{f_2} + L_\theta\left(\frac{\gamma_1-\gamma_2}{f_2}\right) = L_{Be} \text{ (say)}, \quad \text{(A4)}$$

where $f_1 = (1-\gamma_1)$ and $f_2 = (1-\gamma_2)$, and L_{Be} is an effective blackbody radiance. If the radiometer is then calibrated against an external blackbody of radiance L_{ce}, giving a voltage v_c, then using (A3) and (A4) we obtain

$$L_s = L_{Be} - \frac{v_s}{\beta}\frac{1}{f_2} \quad \text{and} \quad L_{ce} = L_{Be} - \frac{v_c}{\beta}\frac{1}{f_2}, \quad \text{(A5)}$$

and

$$v_s = S(L_{Be} - L_s), \quad \text{(A6)}$$

where $S\,(=\beta f_2)$ is defined as a calibration factor. Equation (A6) can be compared with (A2).

Also, from (A5),

$$L_s = L_{Be} - \frac{v_s}{v_c}(L_{Be} - L_{ce}). \quad \text{(A7)}$$

Thus, L_s can be determined independently of f_1 and f_2. However, this is only true if the external ambient temperature remains constant during measurement, otherwise the term in L_θ will change its value and errors will occur. Such errors can be minimized if the term in L_θ vanishes. This will occur if

$$\gamma_1 = \gamma_2. \quad \text{(A8)}$$

In this case, (A7) becomes

$$L_s = L_B\varepsilon_1 - \frac{v_s}{v_c}(L_B\varepsilon_1 - L_{ce}). \quad \text{(A9)}$$

In the case of the ARM radiometer, there is a scanning reflecting mirror to direct the radiance from a source at 45° onto the radiometer aperture. As the reflectance of the mirror will be less than unity, a small mirror emittance ε_m must be considered. Then the radiance at the radiometer aperture is given by

$$L_{se} = (1-\varepsilon_m)L_s + \varepsilon_m L_\theta, \quad \text{(A10)}$$

where L_{se} is an effective source radiance and ε_m is the mirror emittance. The external calibration source will also have an emittance that is less than unity. These emittances must be allowed for when calculating the relevant radiances.

b. Balancing the radiometers

Both the ARM and CSIRO Mark II radiometers were initially balanced before shipment to Kavieng. The optical focusing and alignment systems were adjusted until the output voltage v_c was zero when the external blackbody temperature was equal to the reference blackbody temperature. The balances were checked again in the field, and whereas the ARM radiometer stayed within balance, the CSIRO Mark II radiometer was found to be no longer correctly nulled. This introduced a temperature-dependent term into the calibration and observation equations of (A5). Resultant errors in the calculated radiance are discussed below.

APPENDIX B

Estimation of Errors

a. Errors in the infrared emittance and optical depth

Errors in the infrared cloud absorption radiance can be discussed in terms of (11) and (14). From (11), the theory of errors gives the maximum error in L_a as

$$\max|\Delta L_a| = \Delta L_c + \Delta L_{sc} + \Delta L_r, \quad \text{(B1)}$$

and from (14), the maximum error in L_c as

$$\max|\Delta L_c| = \Delta L_s/\tau + \Delta L_{\text{sky}}/\tau + L_c\Delta\tau/\tau. \quad \text{(B2)}$$

Errors in the measurement of L_s in (14) can be separated into two classes: random electrical noise on the output signal voltage and errors in the calibration of the signal.

Random errors were estimated from the root-mean-square random noise voltage on the signal during a calibration cycle, with constant input radiance. The minimum detectable radiance was then calculated from the signal to noise ratio. Values for the CSIRO Mark II and ARM radiometers are listed in Table 1. The following analysis applies to the CSIRO Mark II radiometer as most of the data were taken with that instrument.

Values of ΔL_{sky} in (B2) contained the same random electronic components as L_s. However, L_{sky} was usually averaged over at least 90 seconds, when conditions were considered to be steady. This was equivalent to a reduction in noise level of a factor of 3 over that of L_s. Errors in τ were related to the random errors in L_{sky} (14).

Random variations in the water vapor radiance L_{sky} were reduced considerably in the present study through the correlation of the clear-sky radiance with the water vapor path (see section 5a). As shown in Fig. 4, these variations can be up to 0.2 W m^{-2} sr^{-1} in the medium term or about six times the random noise in the CSIRO Mark II radiometer.

Errors in the signal calibration had two main causes.

TABLE B1. Fractional errors in calculated cloud radiance L_c for various errors in the effective blackbody radiance L_{Be}.

Percent error in L_{Be}	Percent error in L_c liquid nitrogen	Percent error in L_c ice/water
3.3	7.8	−4.6
6.7	16.2	−8.9
10.0	25.4	−13.0

First, the effective brightness temperatures of the liquid nitrogen and ice/water calibration sources were observed to vary slightly from the specified values of 77 K and 273 K. In the former case, the temperature increased when an ice fog formed above the surface of the liquid nitrogen under windy conditions. This caused a positive deviation of about 1 K unless special care was taken to remove drafts. In the latter case, tests indicated that the ice–water mixture could show a maximum positive deviation of about 0.5 K from 273 K.

The second source of error in the calibration was due to changes in ambient temperature during observations. This occurred because the CSIRO Mark II radiometer optical system was out of balance (see section Ab). The calculated value of L_s could then be greater or less than the correct value [see (A7)]. This would depend on whether the terms L_{Be} and ν_s/ν_c were greater or less than the correct values. As L_s, L_{sky}, and τ were all affected by these systematic errors, the total errors were estimated by considering finite deviations in (14),

$$L_c' - L_c = \frac{\tau(L_s' - L_{\text{sky}}') - \tau'(L_s - L_{\text{sky}})}{\tau\tau'}, \quad \text{(B3)}$$

where the quantities marked with a prime refer to those calculated with an effective blackbody radiance, L_{Be}. Errors in L_c for given errors in L_{Be} are shown in Table B1 for two different calibration sources. The errors from the liquid nitrogen source are seen to be greater than those using the ice/water source. In the former case, errors in L_{sky} reinforce the errors in τ, whereas for the latter, the errors partially balance.

Values of L_{Be} were obtained using an external variable-temperature calibration source at the end of the PROBE experiment. Here L_{Be} was found to be 6.8 W m^{-2} sr^{-1}, which was 0.8 W m^{-2} sr^{-1} above the specified value for a reference blackbody at 40°C. Now, the value of L_{Be} had also been estimated earlier in the experiment when the two radiometers were compared on 26 and 29 January. The Mark II and ARM radiometer radiances were compared and L_{Be} varied until agreement was reached. The value of L_{Be} was then found to be 6.2 W m^{-2} sr^{-1}. The ARM radiometer and NOAA/ETL interferometer radiances were found to agree over the same period (see section 4b), allowing confidence in the calibration of the ARM radiometer. Between 29 January and 3 February, the Mark II radiometer was moved. It was assumed that this was when the optical balance shifted, causing the value of L_{Be} to increase to 6.8 W m^{-2} sr^{-1}. This assumption was corroborated by comparison of the calculated and theoretical values of clear-sky radiances shown in Fig. 2. There was minimum discrepancy between measured and calculated values on 3 and 4 February when the value of L_{Be} was changed to 6.2 W m^{-2} sr^{-1}. Dry-bulb screen temperatures measured during the experiment indicated that temperatures deviated by about 2°C during the daytime periods of measurement. This would be equal to a shift in L_{Be} of 0.3 W m^{-2} sr^{-1}, but most observations were taken with very similar temperatures.

TABLE B2. Fractional errors in the various quantities used to determine errors in L_a and ε_a. Values of L are in W m^{-2} sr^{-1}.

Emittance ε_a		Temperature (°C)		
		−80	−60	−40
All	τ	0.433	0.433	0.433
All	L_{sky}	2.5	2.5	2.5
All	ΔL_s	0.03	0.03	0.03
0.1	L_a	0.041	0.080	0.138
0.1	L_r	0.039	0.039	0.039
0.1	ΔL_c	0.090	0.092	0.102
0.1	ΔL_r	0.0016	0.0016	0.0016
0.1	ΔL_a	0.092	0.094	0.104
0.1	$\Delta L_a/L_a = \Delta\varepsilon_a/\varepsilon_a$	2.25	1.17	0.75
0.5	L_a	0.2	0.4	0.69
0.5	L_r	0.127	0.127	0.127
0.5	ΔL_c	0.112	0.137	0.175
0.5	ΔL_r	0.0051	0.0051	0.0051
0.5	ΔL_a	0.117	0.142	0.180
0.5	$\Delta L_a/L_a = \Delta\varepsilon_a/\varepsilon_a$	0.58	0.35	0.26
0.9	L_a	0.369	0.72	1.242
0.9	L_r	0.145	0.145	0.145
0.9	ΔL_r	0.0058	0.0058	0.0058
0.9	ΔL_c	0.132	0.180	0.259
0.9	ΔL_a	0.138	0.186	0.265
0.9	$\Delta L_a/L_a = \Delta\varepsilon_a/\varepsilon_a$	0.37	0.26	0.21

The total estimated errors are summarized in Table B2. Fractional errors in ε_a were quite large but decreased with increasing temperature and emittance. Errors were reduced by averaging the data within temperature intervals. The high errors were due both to the degradation in signal to noise ratio of the Mark II radiometer output signal and to errors introduced through the out-of-balance condition of the radiometer.

b. Errors in the integrated backscatter, backscatter to extinction ratio, and visible optical depth

Based upon inspection of the recorded cloud signals, observational errors in the values of $B_c'(\pi, z)$, due to photon and electrical noise and the resolution of the digitizer, were estimated to be less than 1%. In addition, the mean error in $B_c'(\pi, z)$, due to day-to-day variations in the lidar calibration, was estimated in section 4a as 14%. Besides the calibration and random errors, the error in the retrieval of the cloud backscatter coefficient $B_c(\pi, z)$ can become large at high optical depths. Small errors in $k/2\eta$ can then cause large errors in $B_c(\pi, z)$, causing equivalent errors in δ_a and δ_c.

Random errors in $k/2\eta$ will mirror those found in

$B'_c(\pi, z)$ and $\gamma'(\pi)$, with an additional uncertainty due to estimation of the value of $\gamma'(\pi)$ when the emittance tends to unity. This error is estimated as $\pm 5\%$. As the function for $k/2\eta$ shown in Table 3 is actually used in the retrievals, there are further errors in estimating the value of $k/2\eta$ at any temperature. These are estimated as $\pm 15\%$.

Resultant errors in the visible optical depth δ_c vary from about 20% to over 50% for optical depths of 0.5 and 5 respectively (P1).

Additional uncertainties will result in the estimation of k through errors in the specified values of η. Total uncertainties are shown in parentheses in Table 3. The equivalent errors in $2\alpha\eta$ and α are indicated similarly in Table 3.

REFERENCES

Ansmann, A., U. Wandinger, M. Riebesell, C. Weitkamp, and W. Michaelis, 1992: Independent measurement of extinction and backscatter profiles in cirrus clouds by using a combined Raman elastic-backscatter lidar. *Appl. Opt.,* **31,** 7113–7131.

Arking, A., and D. Ziskin, 1994: Relationship between clouds and sea surface temperatures in the western tropical Pacific. *J. Climate,* **7,** 988–1000.

Bignell, K. J., 1970: The water vapor infrared continuum. *Quart. J. Roy. Meteor. Soc.,* **96,** 390–403.

Burch, D. E., 1970: Investigation of the absorption of infrared radiation by atmospheric gases. Semiannual Tech. Rep. U-4784, Aeronutronic Division, Philco-Ford Corporation, Newport Beach, CA.

Cess, R. D., L. Potter, J.-P. Blanchet, G. J. Boer, A. D. Del Genio, M. Deque, V. Dymnikov, V. Galin, W. L. Gates, S. J. Ghan, J. T. Kiehl, A. A. Lacis, H. Le Treut, Z.-X. Li, H.-Z. Liang, B. J. McAvaney, V. P. Meleshko, J. F. B. Mitchell, J.-J. Morcrette, D. A. Randall, L. Rikus, E. Roeckner, J. F. Royer, U. Schlese, D. A. Sheinin, A. Slingo, A. P. Sokolov, K. E. Taylor, W. M. Washington, R. T. Wetherald, I. Yagai, and M. H. Zhang, 1990: Intercomparison and interpretation of climate feedback processes in 19 atmospheric general circulation models. *J. Geophys. Res.,* **95,** 16 601–16 615.

Clough, S. A., F. X. Kneizys, and R. W. Davies, 1989: Line shape and the water vapour continuum. *Atmos. Res.,* **23,** 229–241.

Davis, P. A., 1971: Applications of an airborne ruby lidar during a BOMEX program of cirrus observations. *J. Appl. Meteor.,* **10,** 1314–1323.

Fernald, F. G., 1984: Analysis of atmospheric lidar observations: Some comments. *Appl. Opt.,* **23,** 652–653.

Griffith, K. T., S. K. Cox, and R. G. Knollenberg, 1980: Infrared radiative properties of tropical cirrus clouds inferred from aircraft measurements. *J. Atmos. Sci.,* **37,** 1077–1087.

Heymsfield, A. J., 1986: Ice particles observed in a cirriform cloud at −83°C and implications for polar stratospheric clouds. *J. Atmos. Sci.,* **43,** 851–855.

——, and C. M. R. Platt, 1984: A parameterization of the particle size spectrum of ice clouds in terms of ambient temperature and the ice water content. *J. Atmos. Sci.,* **41,** 846–855.

——, and G. M. McFarquhar, 1996: High albedoes of cirrus in the Tropical Pacific Warm Pool: Microphysical interpretation from CEPEX and from Kwajalein, Marshall Islands. *J. Atmos. Sci,* **53,** 2424–2451.

Knollenberg, R. G., K. Kelly, and J. C. Wilson, 1993: Measurements of high number densities of ice crystals in the tops of tropical cumulonimbus. *J. Geophys. Res.,* **98,** 8639–8664.

Lee, A. C. L., 1973: A study of the continuum absorption within the 8–13 μm atmospheric window. *Quart. J. Roy. Meteor. Soc.,* **99,** 490–505.

Macke, A., 1993: Scattering of light by polyhedral ice crystals. *Appl. Opt.,* **32,** 2780–2788.

Minnis, P., D. F. Young, K. Sassen, J. M. Alvarez, and C. J. Grund, 1990: The 27–28 October 1986 FIRE IFO Cirrus Case Study: Cirrus parameter relationships derived from satellite and lidar data. *Mon. Wea. Rev.,* **118,** 2402–2425.

Mitchell, D. L., and W. P. Arnott, 1994: A model predicting the evolution of ice particle size spectra and radiative properties of cirrus clouds. Part II: Dependence of absorption and extinction on ice crystal morphology. *J. Atmos. Sci.,* **51,** 817–832.

Pal, S. R., A. I. Carswell, I. Gordon, and A. Fong, 1995: Lidar-derived cloud optical properties obtained during the ECLIPS program. *J. Appl. Meteor.,* **34,** 2388–2399.

Platt, C. M. R., 1971: A narrow-beam radiometer for atmospheric radiation studies. *J. Appl. Meteor.,* **10,** 1307–1313.

——, 1973: Lidar and radiometric observations of cirrus clouds. *J. Atmos. Sci.,* **30,** 1191–1204.

——, 1978: Lidar backscatter from horizontal ice crystal plates. *J. Appl. Meteor.,* **17,** 482–488.

——, 1979: Remote sounding of high clouds. Part I: Calculation of visible and infrared optical properties from lidar and radiometer measurements. *J. Appl. Meteor.,* **18,** 1130–1143.

——, 1981: Remote sounding of high clouds. Part III: Monte Carlo calculations of multiple scattered lidar returns. *J. Atmos. Sci.,* **38,** 156–167.

——, 1997: A parameterization of the visible extinction coefficient of ice clouds in terms of the ice/water content. *J. Atmos. Sci.,* **54,** 2083–2098.

——, and G. L. Stephens, 1980: The interpretation of remotely sensed high cloud emittances. *J. Atmos. Sci.,* **37,** 2314–2322.

——, and A. C. Dilley, 1981: Remote sounding of high clouds. Part IV: Observed temperature variations in cirrus optical properties. *J. Atmos. Sci.,* **38,** 1069–1082.

——, and Harshvardhan, 1988: Temperature dependence of cirrus extinction: Implications for climate feedback. *J. Geophys. Res.,* **93,** 11 051–11 058.

——, A. C. Dilley, J. C. Scott, I. J. Barton, and G. L. Stephens, 1984: Remote sounding of high clouds. Part V: Infrared properties and structure of tropical thunderstorm anvils. *J. Climate Appl. Meteor.,* **23,** 1296–1308.

——, J. C. Scott, and A. C. Dilley, 1987: Remote sounding of high clouds. VI: Optical properties of mid-latitude and tropical cirrus. *J. Atmos. Sci.,* **44,** 729–747.

——, J. D. Spinhirne, and W. D. Hart, 1989: Optical and microphysical properties of a cold cirrus cloud: Evidence for regions of small ice particles. *J. Geophys. Res.,* **94,** 11 151–11 164.

——, J. W. Bennett, S. A. Young, M. D. Fenwick, P. J. Manson, G. R. Patterson, and B. Petraitis, 1993: Narrow-beam fast filter radiometry and the use of the lidar/radiometer method in the Atmospheric Radiation Measurement Program. *Proc. 3rd Atmos. Radiation Measurement (ARM) Science Team Meeting,* Norman, OK, U.S. Dept. of Energy, 293–297.

Prabhakara, C., J.-M. Yoo, G. Dalu, and D. P. Kratz, 1991: Optically thin cirrus clouds over oceans and possible impact on sea surface temperature of Warm Pool in Western Pacific. NASA Tech. Memo. No. 104550, 36 pp. [Available from Goddard Space Flight Center, Greenbelt, MD 20771.]

Ramanathan, V., and W. Collins, 1991: Thermodynamic regulation of ocean warming by cirrus clouds deduced from observations of the 1987 El Nino. *Nature,* **351,** 27–32.

Ramaswamy, V., and V. Ramanathan, 1989: Solar absorption by cirrus clouds and the maintenance of the tropical upper troposphere thermal structure. *J. Atmos. Sci.,* **46,** 2293–2310.

Roberts, R. E., J. E. A. Selby, and L. M. Biberman, 1976: Infrared continuum absorption by atmospheric water vapor in the 8–12 μm window. *Appl. Opt.,* **15,** 2085–2090.

Roeckner, E., 1988: Cloud-radiation feedbacks in a climate model. *Atmos. Res.,* **21,** 293–303.

Sassen, K., 1992: Evidence for liquid phase cirrus cloud formation from volcanic aerosols: Climatic implications. *Science,* **257,** 516–519.

——, and B. S. Cho, 1992: Subvisual-thin cirrus lidar dataset for satellite verification and climatological research. *J. Appl. Meteor.,* **31,** 1275–1286.

——, C. J. Grund, J. D. Spinhirne, R. M. Hardesty, and J. M. Alvarez, 1990: The 27–28 October 1986 FIRE IFO Cirrus Case Study: A five lidar overview of cloud structure and evolution. *Mon. Wea. Rev.,* **118,** 2288–2311.

Shaw, J. A., J. B. Snider, J. H. Churnside, and M. D. Jacobson, 1995: Comparison of infrared atmospheric brightness temperatures measured by a Fourier transform spectrometer and a filter radiometer. *J. Atmos. Oceanic Technol.,* **12,** 1124–1128.

Spinhirne, J. D., and W. D. Hart, 1990: Cirrus structure and radiative parameters from airborne lidar and spectral radiometer observations: The 28 October 1986 FIRE Study. *Mon. Wea. Rev.,* **118,** 2329–2343.

Stephens, G. L., and T. J. Greenwald, 1991: The earth's radiation budget and its relation to atmospheric hydrology: 2. Observations of cloud effects. *J. Geophys. Res.,* **96,** 15 325–15 340.

Takano, Y., and K. N. Liou, 1995: Radiative transfer in cirrus clouds. Part III: Light scattering by irregular ice crystals. *J. Atmos. Sci.,* **52,** 818–837.

Uthe, E. E., and P. B. Russell, 1976: Lidar observations of tropical high altitude cirrus clouds. *Radiation in the Atmosphere,* H. J. Bolle, Ed., Science Press, 242–244.

Wang, P.-H., M. P. McCormick, L. R. Poole, W. P. Chu, G. K. Yue, G. S. Kent, and K. M. Skeens, 1994: Tropical high cloud characteristics derived from SAGE II extinction measurements. *Atmos. Res.,* **34,** 53–83.

Westwater, E. R., J. H. Churnside, J. A. Shaw, J. B. Snider, K. S. Gage, Y. Han, W. Ecklund, A. Riddle, and A. C. Williams, 1995: Ground-based remote sensor observations during the PROBE experiment in the tropical western Pacific. *Proc. IGARSS '95,* Florence, Italy, IEEE, 882–886.

Yang, P., and K. N. Liou, 1996: Finite-difference time domain method for light scattering by small ice crystals in three-dimensional space. *J. Opt. Soc. Amer. A.,* **13,** 2072–2085.

Young, L. A., 1984: Atmospheric transmittance determination from sky radiance in real time in the tropics. *Appl. Opt.,* **23,** 396–401.

Young, S. A., 1995: Analysis of lidar backscatter profiles in optically thin clouds. *Appl. Opt.,* **34,** 7019–7031.